Supplement of

Three decades of grassland canopy cover change in China (1990-2023) revealed by high-resolution mapping using extensive drone and Landsat data

Xuanhao Jiang, Tianyu Hu, Zhenying Huang, Zhiyao Tang, Leiyi Chen, Wenli Chen, Xiaoli Cheng, Yunxiang Cheng, Yuejun Fan, Ruiru Gao, Tiangang Gao, Yanming Gong, Yanpei Guo, Xiaokang Hu, Chengjun Ji, Liping Li, Shijin Li, Guofang Liu, Wanyin Luo, Hongyuan Ma, Wenhong Ma, Xiujuan Qiao, Chuangye Song, Guoyan Wang, Lei Wang, Qinggang Wang, Yonghui Wang, Zhong Wang, Xuejun Yang, Yan Yang, Yongchuan Yang, Xuehua Ye, Chunying Yin, Feihai Yu, Pujin Zhang, Shuren Zhang, Chengyang Zheng, Luhong Zhou, Yanjun Su

Correspondence to: Yanjun Su (ysu@ibcas.ac.cn)

This file includes:

Tables S1 to S3

Figures S1 to S10

Table S1. The random forest (RF) model parameter settings

Parameter	Setting	Description
n_estimators	100	Number of trees in the forest
max_features	2	Features considered per split
min_samples_split	10	Minimum samples required to split a node
max_depth	8	Maximum tree depth

Table S2. The extreme gradient boosting (XGBoost) model parameter settings

Parameter	Setting	Description
n_estimators	2000	Number of boosting trees
learning_rate	0.1	Step size shrinkage per tree
max_depth	6	Maximum tree depth
min_child_weight	5000	Minimum instance weight per child node
subsample	0.5	Fraction of samples per tree
colsample_bytree	0.8	Fraction of features per tree
reg_alpha	0.0	L1 regularization term
reg_lambda	1.0	L2 regularization term
tree_method	hist	Histogram-based tree construction

Table S3. Summary of existing grassland canopy cover products used for comparison in this study.

Dataset	Regions	Temporal scope	Resolution	Sources
MultiVI FVC	China	2010-2020 (15 day)	30 m	Zhao et al., 2023
MODIS VCF	Global	2000-2020 (Annual)	250 m	DiMiceli et al., 2022
China FVC	China	2000-2024 (Monthly)	250 m	Gao et al., 2022

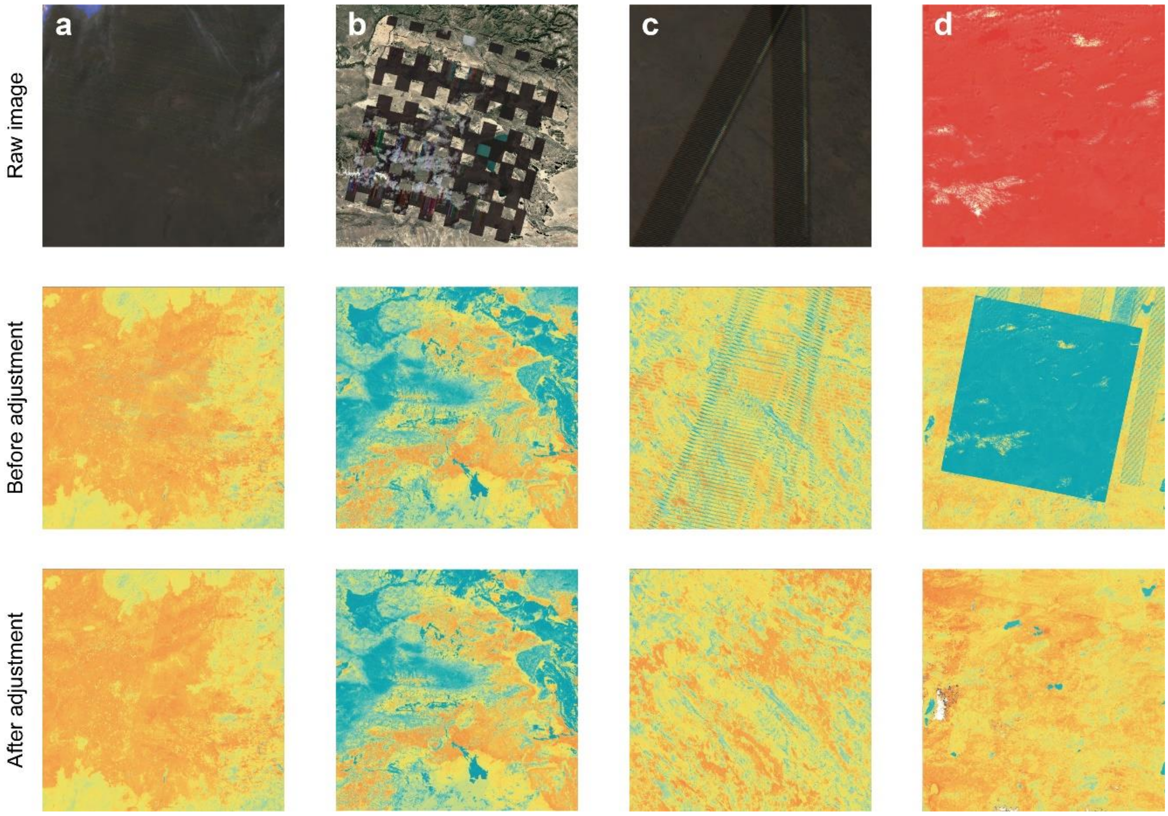

Fig. S1. Visual comparison of annual maximum-value composites of Landsat imagery before and after filtering and inter-mission harmonization. Images are shown in false-color composites. The columns highlight representative sensor-related anomalies: (a) detector failures, (b) solid-state recorder (SSR) bad blocks, (c) shutter synchronization anomalies, and (d) sporadic band anomalies.

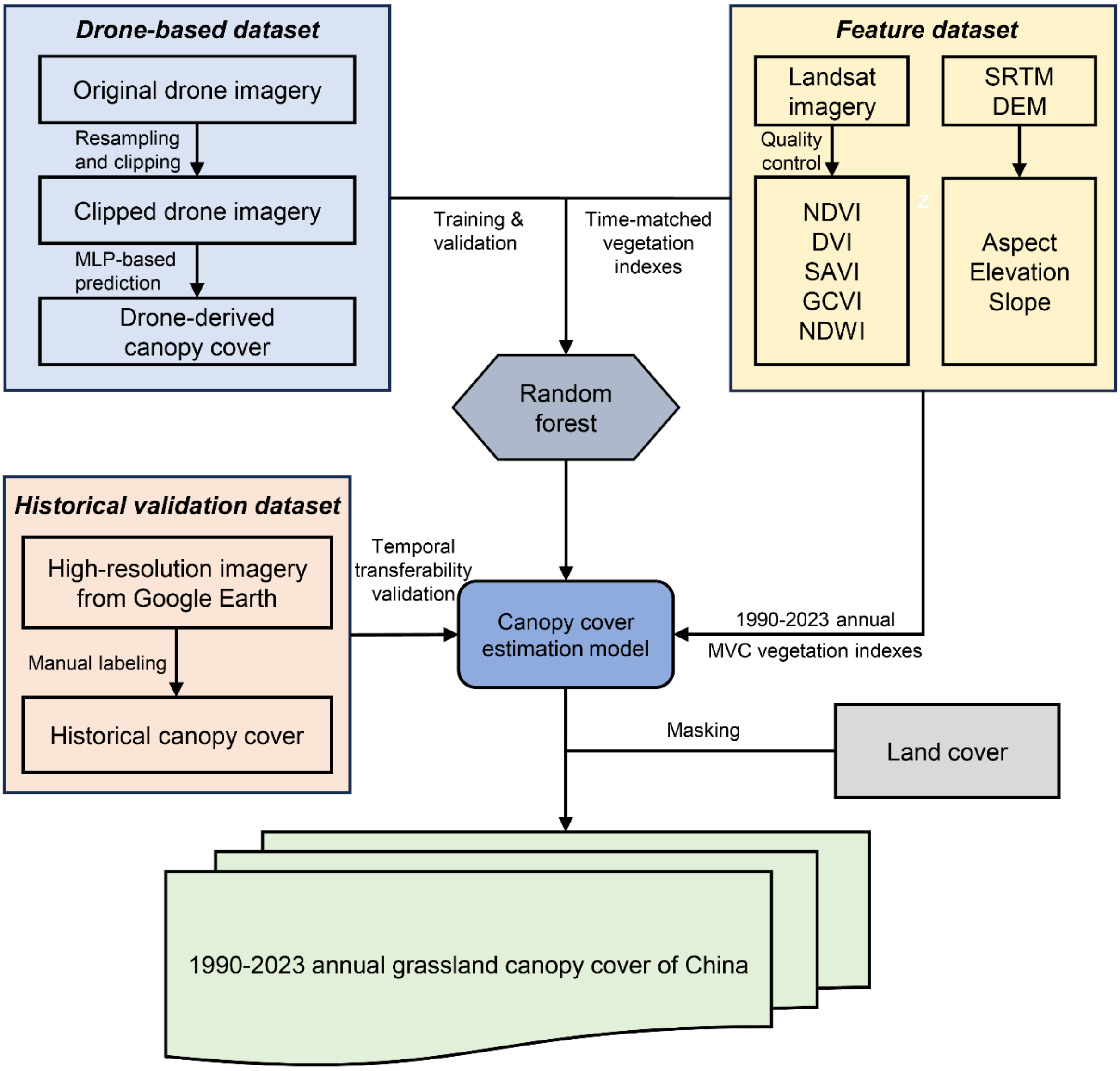

Fig. S2. Overall workflow for mapping annual grassland canopy cover across China from 1990 to 2023.

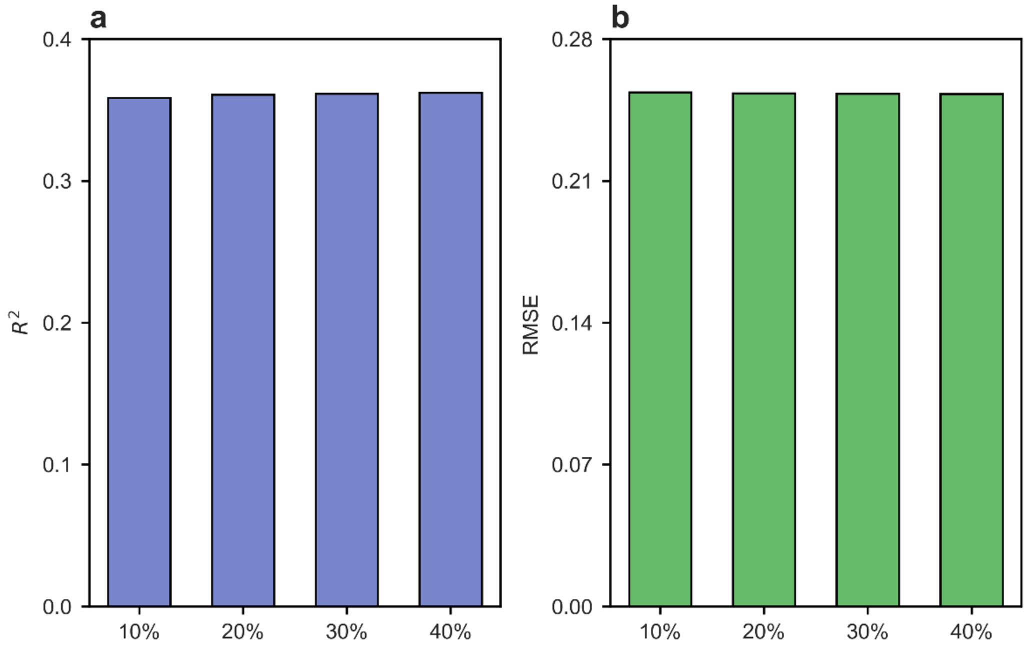

Fig. S3. Performance of the XGBoost model for Shapley Additive Explanations (SHAP) analysis under different sampling ratios. (a) Coefficient of determination (R^2) and (b) root mean squared error (RMSE) for models trained using 10%, 20%, 30%, and 40% of the dataset.

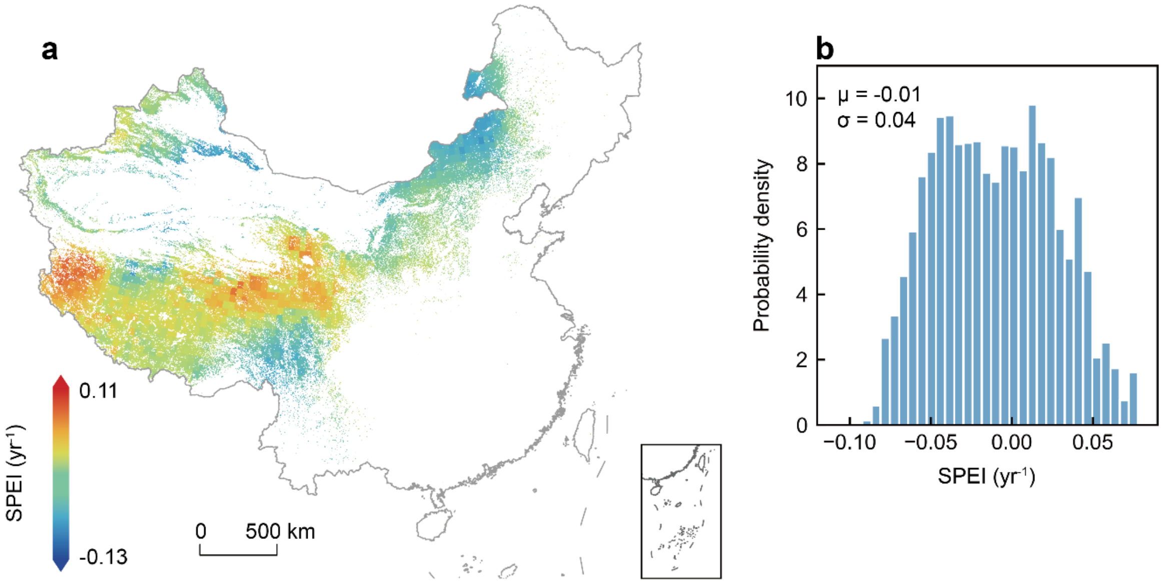

Fig. S4. Spatial distribution and statistical characteristics of standardized precipitation–evapotranspiration index (SPEI) trends in China's grasslands from 1990 to 2020. (a) Spatial pattern of the SPEI trend. (b) Probability density distribution of SPEI trends. μ and σ denote the mean and standard deviation, respectively.

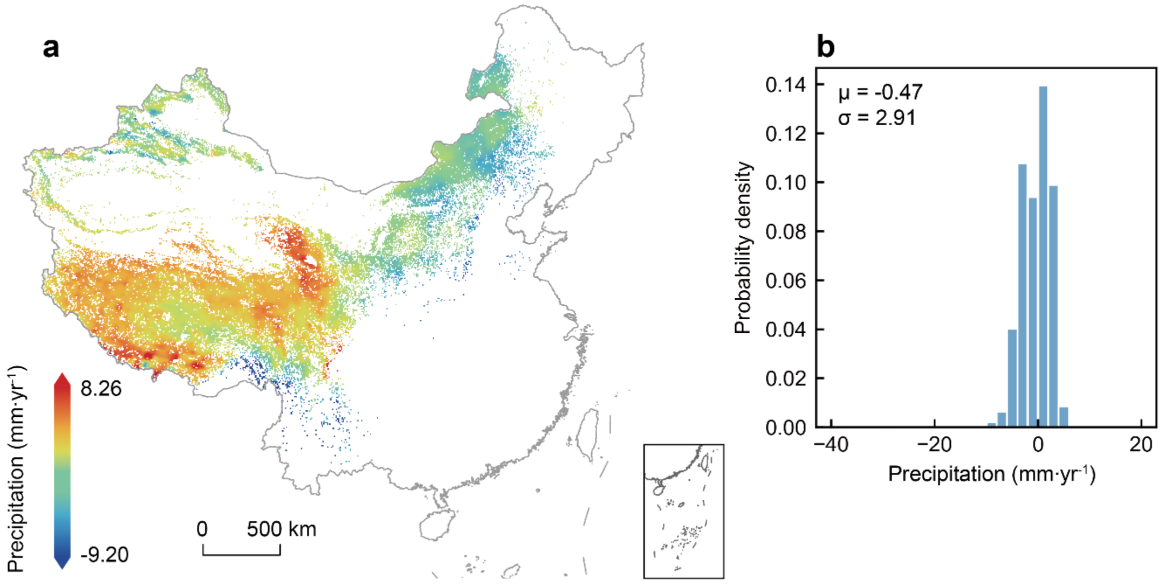

Fig. S5. Spatial distribution and statistical characteristics of precipitation trends in China's grasslands from 1990 to 2020. (a) Spatial pattern of the mean annual total precipitation trend. (b) Probability density distribution of mean annual total precipitation trends.

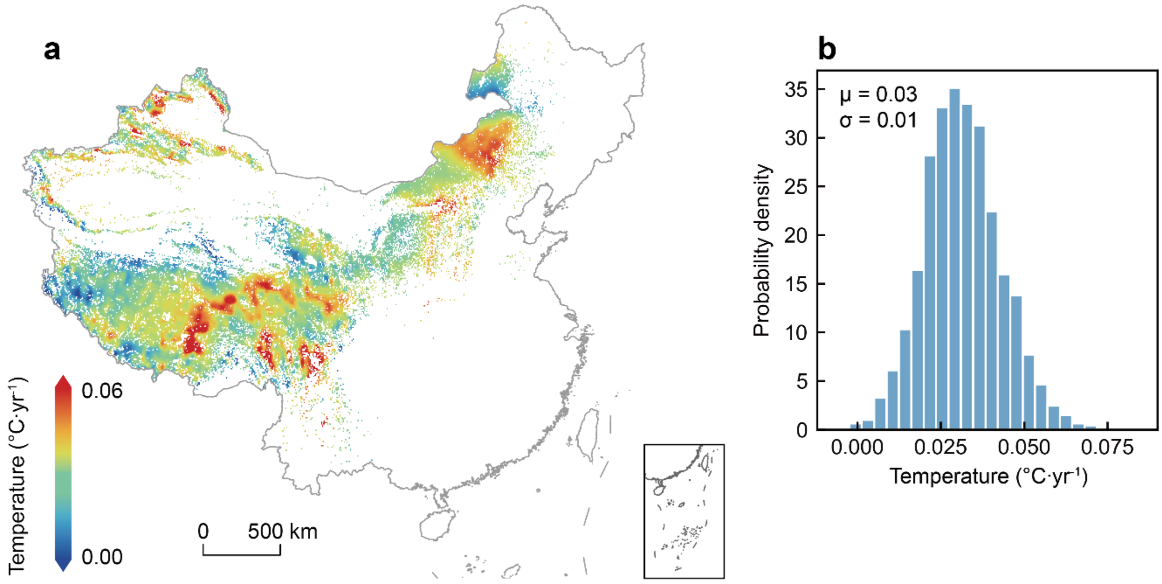

Fig. S6. Spatial distribution and statistical characteristics of temperature trends in China's grasslands from 1990 to 2020. (a) Spatial pattern of the mean annual temperature trend. (b) Probability density distribution of mean annual temperature trends.

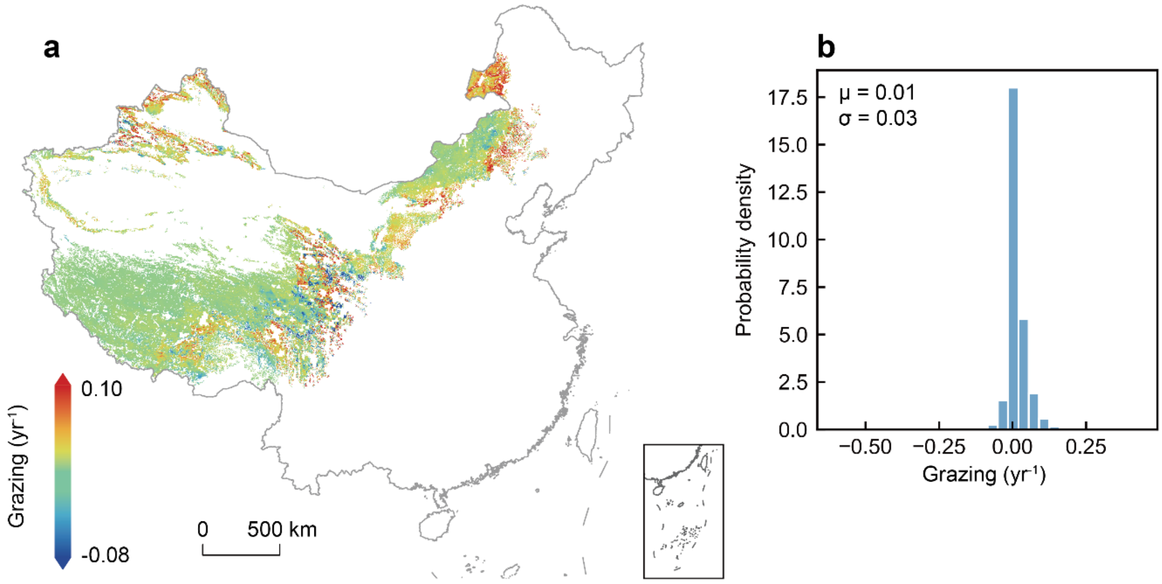

Fig. S7. Spatial distribution and statistical characteristics of grazing trends in China's grasslands from 1990 to 2020. (a) Spatial pattern of the grazing intensity trend. (b) Probability density distribution of grazing intensity trends.

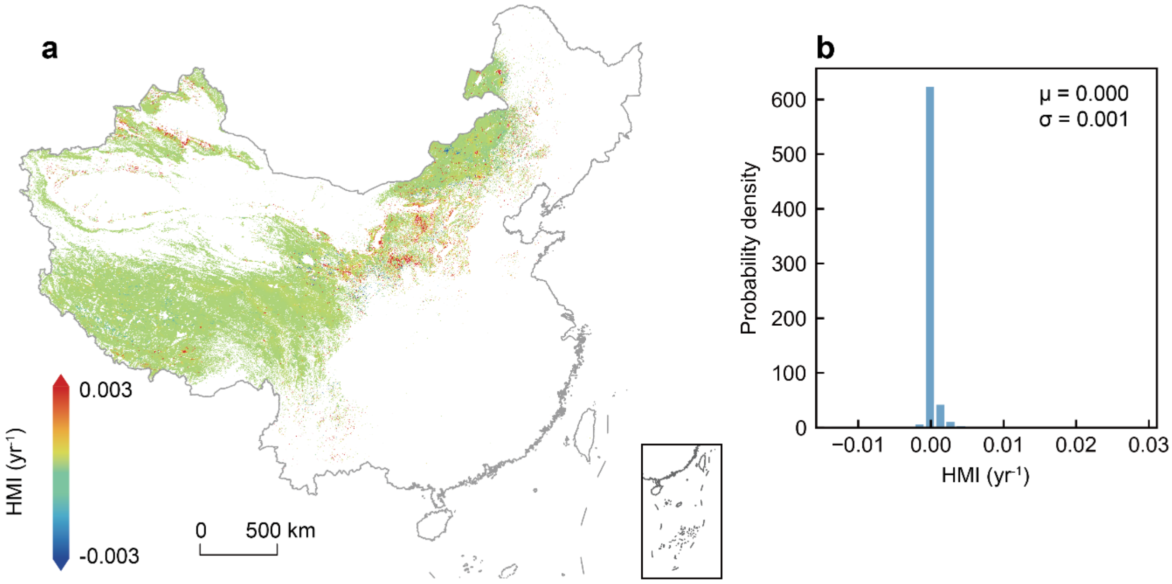

Fig. S8. Spatial distribution and statistical characteristics of human modification index (HMI) trends in China's grasslands from 1990 to 2020. (a) Spatial pattern of the HMI trend. (b) Probability density distribution of HMI trends.

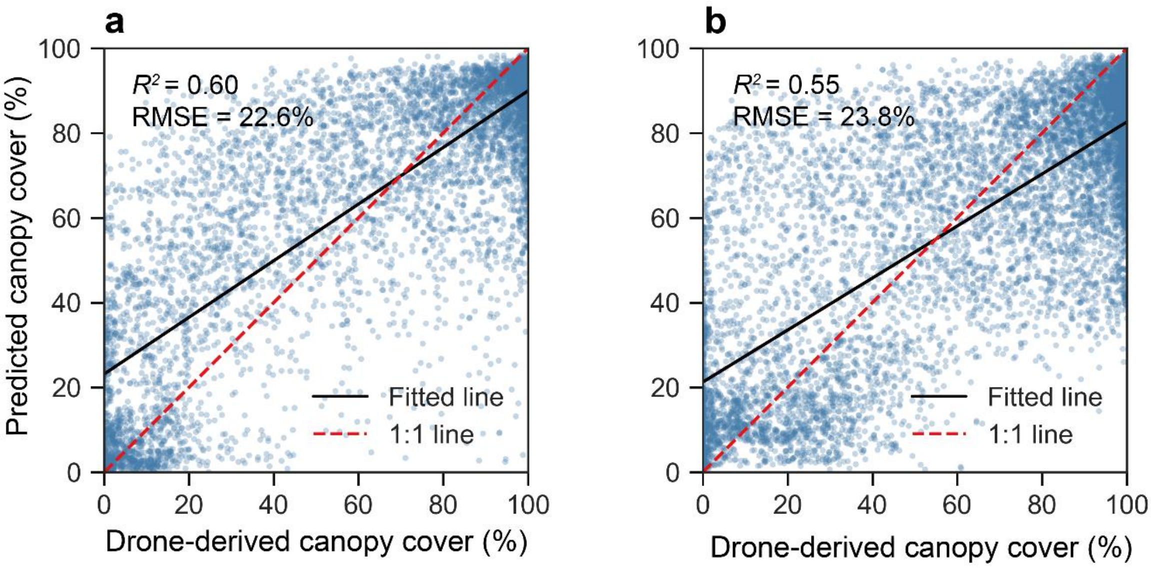

Fig. S9. Assessment of temporal transferability of the RF model trained using (a) 2021 drone imagery and (b) 2022 drone imagery.

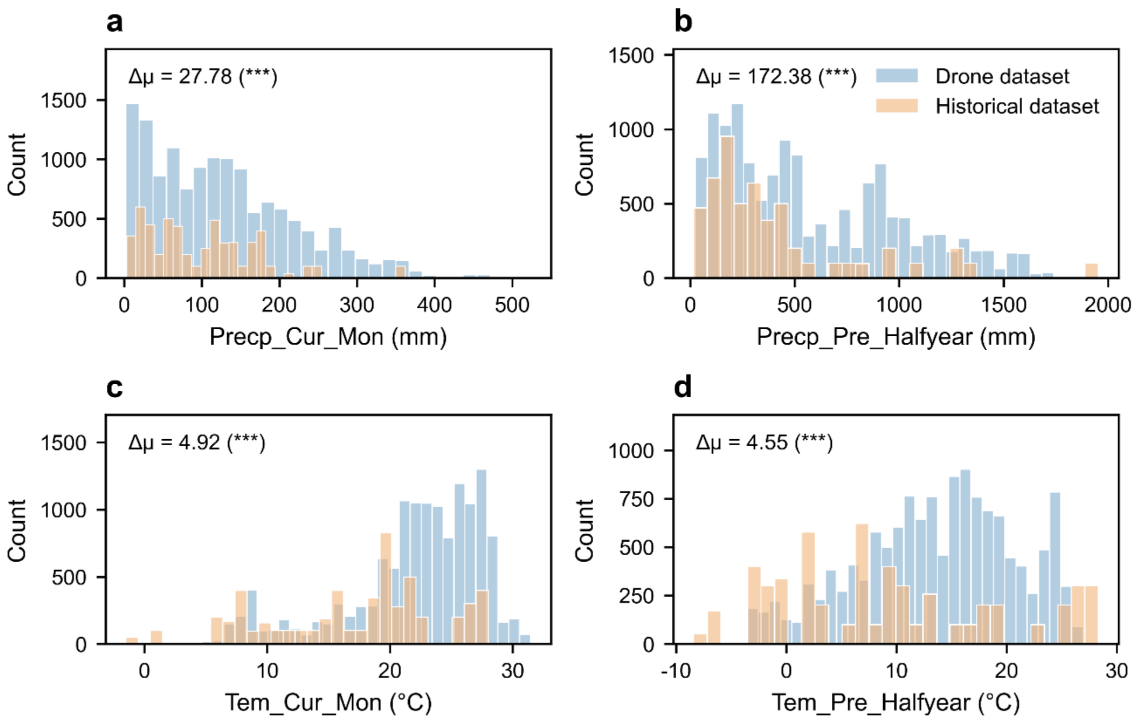

Fig. S10. Histograms of (a) total precipitation during the month of imagery acquisition (Precp_Cur_Mon), (b) total precipitation over the six months preceding drone imagery acquisition (Precp_Pre_Halfyear), (c) mean temperature during the month of imagery acquisition (Tem_Cur_Mon), and (d) mean temperature over the six months preceding imagery acquisition (Tem_Pre_Halfyear). The difference in means (Δμ) between the two datasets and the statistical significance (***, $p < 0.001$) are indicated in each subplot.

References

DiMiceli, C., Sohlberg, R., and Townshend, J.: MODIS/Terra Vegetation Continuous Fields Yearly L3 Global 250m SIN Grid V061, NASA Land Processes Distributed Active Archive Center [data set], https://doi.org/10.5067/MODIS/MOD44B.061, 2022.

Gao, J., Shi, Y., Zhang, H., Chen, X., Zhang, W., Shen, W., Xiao, T., and Zhang, Y.: China regional 250m fractional vegetation cover data set (2000-2024), National Tibetan Plateau Data Center [data set], https://doi.org/10.11888/Terre.tpdc.300330, 2022.

Zhao, T., Mu, X., Song, W., Liu, Y., Xie, Y., Zhong, B., Xie, D., Jiang, L., and Yan, G.: Mapping spatially seamless fractional vegetation cover over China at a 30-m resolution and semimonthly intervals in 2010–2020 based on Google Earth Engine, J. Remote Sens., 3, 0101, https://doi.org/10.34133/remotesensing.0101, 2023.